PAPER

Aerosol-jet-printed graphene electrochemical immunosensors for rapid and label-free detection of SARS-CoV-2 in saliva

To cite this article: Cícero C Pola et al 2022 2D Mater. 9 035016

View the article online for updates and enhancements.

You may also like

- Molecular basis of COVID-19 pathogenesis
 Fedor N. Novikov, Viktor S. Stroylov, Igor V. Svitanko et al.
- Accurate Evaluation on the Interactions of SARS-CoV-2 with Its Receptor ACE2 and Antibodies CR3022/CB6 Hong-ming Ding, , Yue-wen Yin et al.
- Emerging nanotechnology role in the development of innovative solutions against COVID-19 pandemic Zeeshan Ahmad Bhutta, Ayesha Kanwal, Moazam Ali et al.

2D Materials



2 February 2022

REVISED 20 April 2022

ACCEPTED FOR PUBLICATION 24 May 2022

PUBLISHED 10 June 2022

PAPER

Aerosol-jet-printed graphene electrochemical immunosensors for rapid and label-free detection of SARS-CoV-2 in saliva

Cícero C Pola^{1,5}, Sonal V Rangnekar^{2,5}, Robert Sheets¹, Beata M Szydłowska², Julia R Downing², Kshama W Parate¹, Shay G Wallace², Daphne Tsai², Mark C Hersam^{2,3,4,*}, Carmen L Gomes^{1,*} and Jonathan C Claussen1,* [D]

- Department of Mechanical Engineering, Iowa State University, Ames, IA 50011, United States of America
- Department of Materials Science and Engineering, Northwestern University, Evanston, IL 60208, United States of America
- Department of Chemistry, Northwestern University, Evanston, IL 60208, United States of America
- Department of Electrical and Computer Engineering, Northwestern University, Evanston, IL 60208, United States of America
- Contributed equally to this work.
- Authors to whom any correspondence should be addressed.

E-mail: jcclauss@iastate.edu, carmen@iastate.edu and m-hersam@northwestern.edu

Keywords: graphene, biosensor, electrochemical impedance spectroscopy, COVID-19, aerosol jet printing Supplementary material for this article is available online

Abstract

Rapid, inexpensive, and easy-to-use coronavirus disease 2019 (COVID-19) home tests are key tools in addition to vaccines in the world wide fight to eliminate national and local shutdowns. However, currently available tests for SARS-CoV-2, the virus that causes COVID-19, are too expensive, painful, and irritating, or not sufficiently sensitive for routine, accurate home testing. Herein, we employ custom-formulated graphene inks and aerosol jet printing to create a rapid electrochemical immunosensor for direct detection of SARS-CoV-2 spike receptor-binding domain (RBD) in saliva samples acquired noninvasively. This sensor demonstrated limits of detection that are considerably lower than most commercial SARS-CoV-2 antigen tests (22.91 \pm 4.72 pg ml⁻¹ for spike RBD and $110.38 \pm 9.00 \text{ pg ml}^{-1}$ for spike S1) as well as fast response time ($\sim 30 \text{ min}$), which was facilitated by the functionalization of printed graphene electrodes in a single-step with SARS-CoV-2 polyclonal antibody through the carbodiimide reaction without the need for nanoparticle functionalization or secondary antibody or metallic nanoparticle labels. This immunosensor presents a wide linear sensing range from 1 to 1000 ng ml⁻¹ and does not react with other coexisting influenza viruses such as H1N1 hemagglutinin. By combining high-yield graphene ink synthesis, automated printing, high antigen selectivity, and rapid testing capability, this work offers a promising alternative to current SARS-CoV-2 antigen tests.

1. Introduction

Since its first report in December 2019, the coronavirus disease 2019 (COVID-19) pandemic continues to cause enormous human, social, and economic suffering across the globe as over 480 million cases have been reported and over 6.1 million people have died as of April 2022 [1]. The number and severity of cases are a result of the virus's fast rates of human-to-human transmission, which primarily occurs through aerosol droplets, a considerable percentage of asymptomatic patients, and unpredicted virus mutation [2, 3]. During the pandemic, a

number of strategies to combat the spread of COVID-19 such as lockdowns, mask mandates, contact tracing, vaccinations, and diagnostic testing have been implemented with varying rates of success and side effects. Lockdowns have enabled social distancing but have upended the global economy, causing contraction by 3.5% in 2020, and have negatively impacted the social well-being of communities [4–6]. Mask mandates helped control COVID cases but are being lifted in the US as they have been met with personal, political, and legal challenges that make them increasingly difficult to enforce [7-9]. Vaccinations have been key in reducing COVID transmission and

severity of disease, but, for example, 9.0% of fully vaccinated individuals in New York State still experienced breakthrough infections with the Omicron variant [10]. Furthermore, in just over a year since COVID-19 vaccines became available, global vaccine scarcity still prevails—only 15% of people in low-income countries have received at least one dose, while that number is about 80% in upper-middleand high-income countries—and issues of production limitations, export bans, vaccine hoarding, and vaccine hesitancy have caused vaccination rates to plateau globally [11]. On the other hand, diagnostic testing options and the demand for testing have continued to grow and be subsidized by governments in an effort to curb transmission rates. The US launched a service to distribute free rapid test kits in January 2022 [12]. In the face of a major COVID-19 outbreak and consequent lockdown in Shanghai, China in March 2022, government officials implemented mass testing to identify infected individuals that needed to quarantine [13]. Additionally, as international travel restrictions begin to ease, e.g. Australia reopened to vaccinated tourists in February 2022, many countries still require a negative COVID-19 test 24-72 h before entry [14]. Routine and frequent testing also has the potential to lead to better prognosis since those individuals who discover their illness early could take anti-COVID drugs such as Molnupiravir and Paxlovid to significantly reduce the effects of the disease [15, 16]. Thus, there continues to be a need for accessible COVID-19 diagnostic tests that are fast, frequent, and easy-to-use at home without a prescription to facilitate a safe return to pre-pandemic activities.

Frequent at-home testing requires an accurate test that is not only inexpensive and easy-to-use, but also pain-free to avoid testing aversion. Painful nasopharyngeal and oropharyngeal swab tests that sometimes cause bleeding would most likely not be self-administrated regularly [17]. Likewise, tests that use painful finger pricks are suboptimal as they can cause test hesitancy as experienced with the diabetic finger prick test [15]. Several manufacturers have created at-home SARS-CoV-2 tests that use a less painful but still uncomfortable nasal swab to transfer bodily fluid to a lateral flow assay (LFA) capable of detecting nucleocapsid (N) protein antigens from the SARS-CoV-2 virus [16]. Such LFA SARS-CoV-2 antigen tests are too expensive for daily or even weekly testing as they typically cost between \$25 and \$55 a test and can exhibit a high rate of false positives (up to 52% in some cases) [18–20]. Manufacturers have also designed molecular home tests, which utilize loop-mediated isothermal amplification (LAMP) to amplify the RNA of SARS-CoV-2 virus found in a test sample to quantify the viral load [21]. These molecular tests are considered to be more sensitive than the LFA antigen tests as their results rival the

accuracy of the gold-standard real-time quantitative reverse transcription polymerase chain reaction (RT-PCR) laboratory test for diagnosis of SARS-CoV-2 [22]. However, their accuracy seems to significantly wane after the acute symptomatic phase of SARS-CoV-2, and they are more expensive than antigen tests (price ranges close to \$90 per test) due, in part, to the need for LAMP reagent kits and primer sets [21, 22]. Hence, it is likely that molecular tests will remain cost prohibitive for routine at-home testing of SARS-CoV-2. It should be noted here that other serological tests, or tests that monitor antibodies in the blood that have been produced during the immune response to COVID-19, have been developed for home use. However, the U.S. Food and Drug Administration has stated that such tests should not be used to evaluate the level of immunity or protection from SARS-CoV-2 at any time due to their unreliability [23].

To avoid the issues with incumbent COVID-19 surveillance, it would be ideal to develop a rapid, accessible, sensitive, and pain-free at-home COVID-19 test that only requires saliva samples. In this way, users could easily spit inside a disposable test cup and acquire measurements without the need to swab their throat or nose or the need to prick their finger. Studies comparing the detection of SARS-CoV-2 in saliva and nasopharyngeal samples have shown concordance between 94% [24] and 97.4% [25]. Moreover, the presence of SARS-CoV-2 in saliva droplets has also been demonstrated consistently for different stages of the disease and has been used as a reliable SARS-CoV-2 diagnostic tool [24–28]. However, it is imperative that a saliva-based test provides a more quantitative readout than LFAs, which only provide a qualitative, yes/no response that relies upon visual assessment and is unable to quantify specific concentrations of antigen [29]. Moreover, the sensitivity of an LFA can be reduced by nonspecific surface adsorption of reagents, protein denaturation, and steric hindrance since biological molecules interact with the many inorganic-biological surfaces within the porous cellulose membranes as fluid moves from a target line to a control line [30]. On the other hand, electrochemical sensors offer a quantitative and label-free approach to saliva-based diagnostic testing. While electrochemical COVID-19 tests would require access to a portable potentiostat, the cost of which represents the largest threat to adoption in low-income areas, inexpensive smartphone-controlled potentiostats capable of both DC and AC measurements have been developed by several groups in recent years [31–34]. Moreover, the potentiostat would be a one-time investment that could be shared amongst relatives, neighbors, and communities, potentially further lowering the barrier to adoption. Commercial electrochemical biosensors for use in the home have been widely deployed (e.g. home glucose monitoring tests), which suggest

that a suitable electrochemical SARS-CoV-2 home kit would have a high technology adoption [35]. Therefore, the focus of this work is on the development of sensitive, accurate, and inexpensive functionalized electrodes for electrochemical sensing of COVID-19 in saliva samples.

Several groups have recently demonstrated electrochemical sensors for rapid quantification of SARS-CoV-2 antigens in saliva and have focused on monitoring the spike S1 protein. It should be noted that the spike S1 protein is a promising antigen candidate for diagnostic purposes since it is the major transmembrane protein of SARS-CoV-2 and is highly immunogenic. The trimeric spike S1 protein mediates the viral entry in a human cell through the interaction of one of its receptor binding domains (RBDs) with the angiostensin-converting enzyme-2 [36, 37]. Fabiani et al [38] developed an electrochemical immunosensor capable of detecting SARS-CoV-2 nucleocapsid (N) protein and spike S1 protein at concentrations as low as 8 ng ml⁻¹ and 19 ng ml⁻¹ in saliva. This sensor requires a secondary antibody with alkaline phosphatase as an immunological label along with magnetic beads (MBs) to help draw the antigen to a screen-printed carbon electrode surface upon application of a magnetic field. Mahari et al [39] developed an electrochemical immunosensor capable of detecting spike S1 protein with detection limits as low as 10 fM. This sensor also requires the spike antigen to be labeled with Ag nanoparticles to enhance the electrochemical signal output form a screenprinted electrode functionalized with anti-spike protein antibodies. Other reports have focused on developing label-free electrochemical sensors for detecting SARS-CoV-2 protein in saliva, but they require the use of exotic nanotubes and nanoparticles (e.g. titanium nanotubes and copper oxide nanocubes) to enhance the electroactivity of the electrodes [40, 41]. Other researchers have also developed promising and sensitive electrochemical label-free antigen tests using biorecognition agents besides antibodies, such as aptamers, but the production, stability, and reliability of these biorecognition agents are still too uncertain for large-scale implementation [42, 43].

Central to the successful deployment of electrochemical immunosensors is the use of readily scalable materials and manufacturing techniques. In this context, graphene is an excellent electrode material candidate due to its high electrical conductivity, biocompatibility, and large surface area for chemical functionalization [44–46]. However, many graphene sensors require more expensive techniques to synthesize graphene such as chemical vapor deposition (CVD), laser ablation, or epitaxial growth [47–49] and multi-step lithographic patterning, substrate etching, or exfoliation processes [50, 51] to pattern and/or transfer the graphene to a substrate suitable for biosensing. For example, Seo *et al* fabricated

a highly sensitive COVID-19 field-effect transistor (FET) sensor based on a CVD-grown graphene film, which required wet transfer from a Cu foil and photolithographic patterning and etching to define each device [36]. In contrast, solution processing provides a route for obtaining graphene nanosheets in a high throughput and inexpensive manner [52]. Many COVID sensor studies have opted to use reduced graphene oxide (rGO)—produced by way of graphene oxide, which is synthesized inexpensively in large quantities through the modified Hummer's method. Though this method produces a more reactive version of graphene, this material is not conductive enough to serve as an electrode. Studies utilizing rGO for COVID sensors have only deposited rGO on more conductive electrode materials such as Au [37, 53] or glassy carbon electrodes [54–56] to measure electrochemical signals. On the other hand, conductive graphene electrodes fabricated through additive manufacturing techniques such as aerosol jet printing (AJP) and laser scribing have been previously demonstrated for label-free immunosensing of biogenic small molecules, proteins, and pathogens [57–60]. However, recent reports of COVID-19 sensors based on printed or laser-scribed graphene have required more complex processing methods such as sandwich assays [61, 62] or labeling or electrochemical activation by adding Au nanoparticles [63, 64] to enable high-sensitivity to SARS-CoV-2 proteins.

Herein, we report a label-free, high-sensitivity, and rapid-response-time graphene-based electrochemical immunosensor for quantitatively detecting the SARS-CoV-2 spike RBD as well as SARS-CoV-2 spike S1 protein. The AJP graphene immunosensors detect SARS-CoV-2 spike RBD and spike S1 in artificial saliva samples, presenting a limit of detection (LOD) of 22.91 \pm 4.72 pg ml⁻¹ and $110.38 \pm 9.00 \,\mathrm{pg}\,\mathrm{ml}^{-1}$, respectively, after 33 min. This detection limit is considerably lower than commercially available LFA antigen sensors that only exhibit detection limits within the low ng ml⁻¹ range [65]. As the first demonstration of custom-formulated graphene inks for COVID-19 detection, a grapheneethyl cellulose (EC) ink was deposited by AJP onto a polyimide substrate in a dipstick pattern composed of a 3 mm diameter circular working area (figure 1(a)). The printed graphene sensors are subsequently biofunctionalized with a SARS-CoV-2 Rabbit polyclonal antibody via N-(3-dimethylaminopropyl)-N'ethylcarbodiimide (EDC): N-hydroxysuccinimide (NHS) crosslinker (figures 1(b) and (c)). Notably, the electroactivity of the electrode does not need to be enhanced with metallic nanoparticles. In addition, immunological labels, such as a secondary antibody or metallic nanoparticles, are not required, resulting in a COVID-19 testing paradigm in which saliva samples are promptly incubated on the sensor

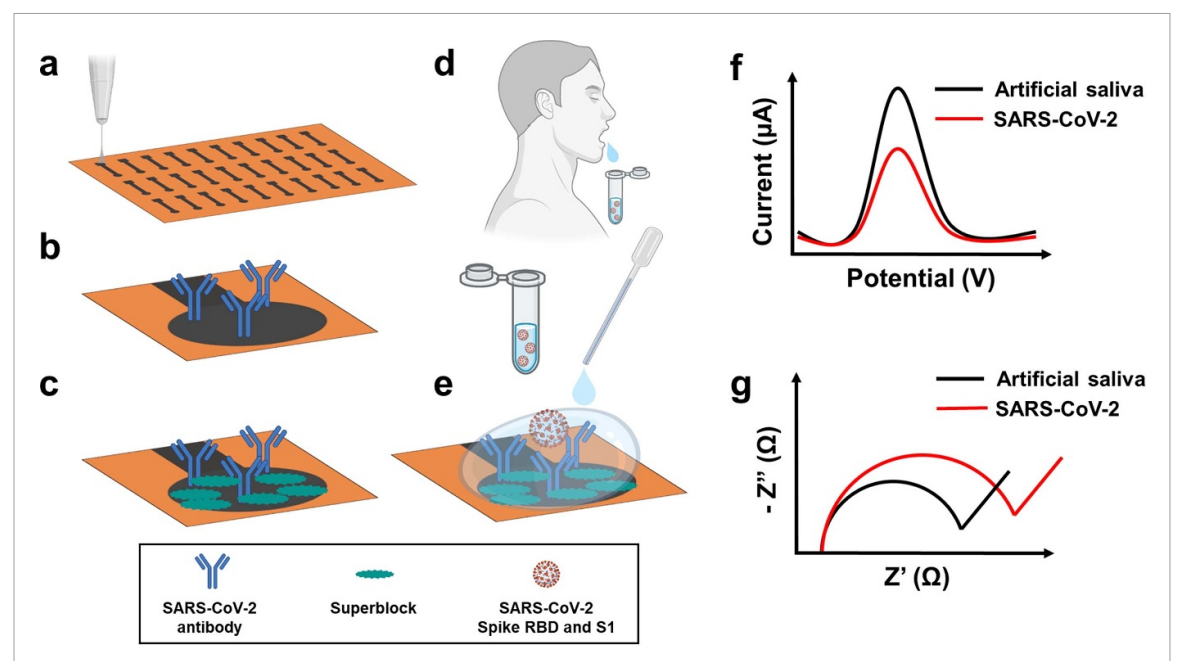


Figure 1. Schematic representation of the fabrication, biofunctionalization, and proposed implementation of the aerosol-jet-printed (AJP) graphene biosensor. (a) AJP of graphene ink in a dipstick pattern on a polyimide substrate. (b) Immobilization of SARS-CoV-2 antibodies on the AJP graphene dipstick surface via carbodiimide cross-linking chemistry. (c) Prevention of nonspecific adsorption onto the sensor in subsequent steps by treating the remaining unfunctionalized areas of the AJP graphene dipstick with blocking agent (Superblock™). (d) Proposed sample collection paradigm in which the saliva sample can be noninvasively obtained from a patient and promptly tested. (e) Incubation of the AJP graphene dipstick biosensor with SARS-CoV-2 virions in a real saliva sample or with SARS-CoV-2 spike S1 or RBD in artificial saliva. (f) and (g) Graphical representation of the resulting changes in the differential pulse voltammetry (DPV) and electrochemical impedance spectroscopy (EIS) signals, respectively, with background signal from artificial saliva (black) and output signal from SARS-CoV-2 spike RBD (red).

after collection (figures 1(d) and (e)). Subsequently, electrochemical sensing techniques, such as differential pulse voltammetry (DPV) and electrochemical impedance spectroscopy (EIS), are performed for quantitative measurement of antigen concentration in the sample (figures 1(f) and (g)).

The materials and processing techniques utilized in this work were chosen for their manufacturing scalability and inexpensiveness. Specifically, EC-coated graphene nanosheets are produced in an automated, continuous-flow process for approximately \$0.02 per gram of graphene (this cost can likely be further reduced by taking advantages of economies of scale at larger production levels). The AJP process also minimizes graphene ink utilization and waste by only depositing graphene into the targeted electrode geometry at thicknesses of ~225 nm. In this manner, this process uses significantly less graphene material than more conventional printing techniques such as inkjet printing [44, 66, 67], screen printing [68], gravure printing [69]), and spin coating coupled with inkjet maskless lithography [70, 71], which yield film thicknesses ranging from a few microns to several tens of microns. Leveraging high-yield batch graphene ink synthesis and high-yield automated printing, we estimate the current cost of our sensors to be \$3.39 each with further cost reductions possible with further scale-up. Thus, the resulting AJP graphene-based immunosensor is a simple, rapid, cost-effective, and

sensitive alternative to currently available COVID-19 antigen tests.

2. Results and discussion

2.1. AJP graphene-based electrode fabrication

The graphene ink used to fabricate the sensors was prepared using a previously described pilot-scale process [56]. Briefly, we performed liquid-phase shear exfoliation of graphite flakes in ethanol using EC as the dispersant and stabilizer polymer. The obtained graphene/EC slurry was further processed to yield a graphene/EC powder containing 40% wt. exfoliated graphene nanosheets. Next, an AJP graphene ink was formulated by redispersing the graphene/EC in 9:1 ethanol:terpineol. During printing, the ink was ultrasonically atomized, and the aerosol droplets were transported by a carrier gas to the deposition head, where a sheath gas is introduced to focus the aerosol stream into a narrow diameter on the substrate [72]. Using this approach, the graphene/EC ink was printed into a dipstick electrode pattern (figure 1(a)) at print speed of 5 mm s⁻¹. Once deposited, the devices were annealed in a box furnace at 350 °C for 30 min to remove any residual solvent trapped in the inner layer of the graphene film [58, 73]. This heat treatment was also used to promote the thermal degradation of the EC into an sp²-rich carbonaceous residue and expose the graphene sheets [44, 57, 74],

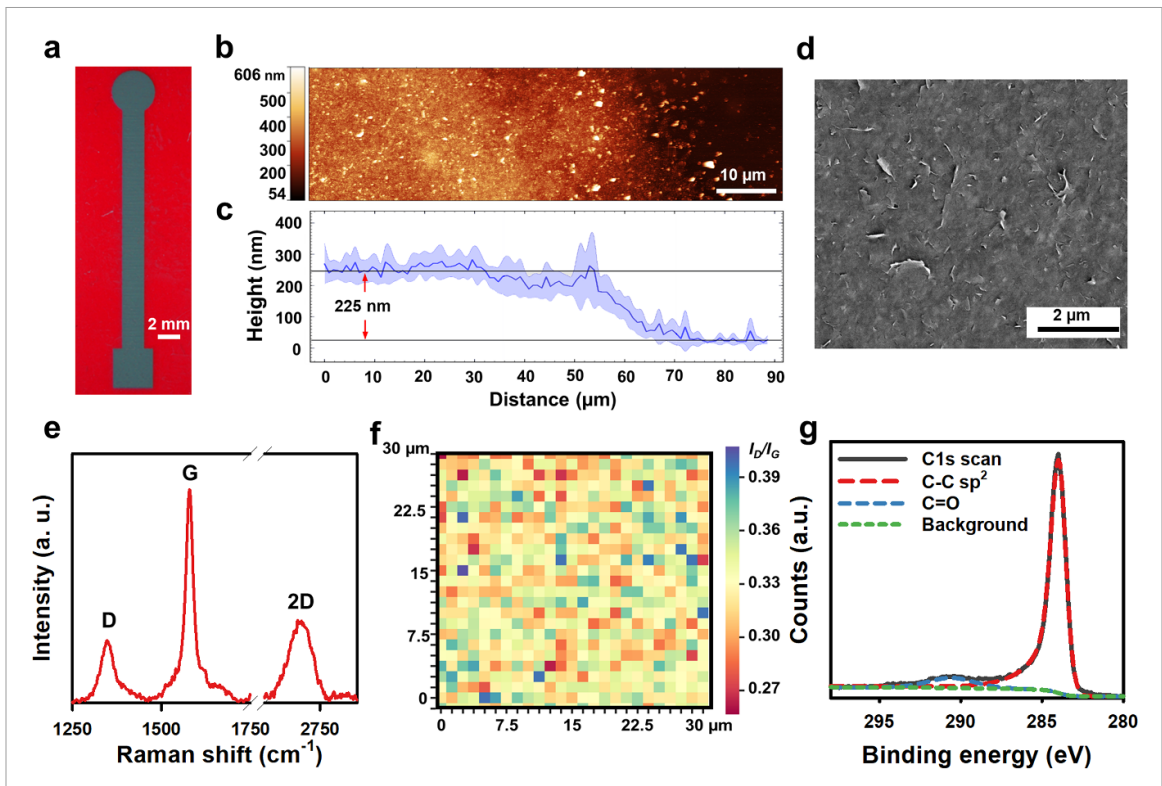


Figure 2. Microscopic and spectroscopic characterization of AJP dipstick electrodes on a polyimide substrate. (a) Optical micrograph at $6.3 \times$ magnification. (b) AFM height map across the cleaned region. (c) Height profile extracted from AFM displaying an average thickness of \sim 225 nm. (d) SEM image revealing the surface topography at 15 000× magnification. (e) Representative Raman spectrum with the characteristic D, G, and 2D modes of graphene. (f) Raman map $(30 \times 30 \ \mu m)$ region) displaying I_D/I_G peak ratio with an average value of 0.33 ± 0.025 . (g) XPS spectrum revealing surface functional groups.

resulting in a material with high electrical conductivity of $1.8 \times 10^4 \pm 1.8 \times 10^3$ S m⁻¹ and a sheet resistance of 240 ± 23 Ω sq⁻¹ (n = 8).

2.2. Microscopy characterization

The AJP graphene electrode morphology was characterized by optical microscopy, atomic force microscopy (AFM), and scanning electron microscopy (SEM) (figure 2). Optical microscopy confirms the deposition of a continuous dipstick electrode with well-defined edges and uniform thickness (figure 2(a)). The electrode was designed as a 3 mm diameter circle connected to a 3×3 mm² contact pad by a 20 mm long stem. The circular working area was defined by applying a passivation layer of insulating fast-drying nitrocellulose-based lacquer [59] on the electrode stem, resulting in a geometric working area of 7.07 mm².

The print morphology was investigated with AFM to quantify the film thickness and surface roughness. First, a section of the printed and cured electrode was gently removed with aid of isopropanol without indenting the polyimide substrate. Then, AFM scans were performed in this region to obtain a height map of the pristine printed graphene film in comparison to the cleaned area (figures 2(b) and (c)). The printed graphene film was measured to have a thickness of approximately 225 nm. It is important to note that a wide scanning window (90 μ m) was

necessary to obtain accurate height values, as a narrower window led to thickness underestimation due to partial distortion of the printed film at the border of the pristine print and cleaned surface. Additionally, AFM scans of pristine portions of the AJP electrode revealed a film roughness of approximately 35 nm, averaged over four scans. Similar film roughness values (37 nm) were previously observed during the fabrication of interdigitated electrodes using nitrocellulose-based graphene inks through the same technique [58], demonstrating consistency in the printing process despite the use of different cellulose-based binders.

SEM images revealed that the AJP graphene film consists of a dense network of graphene nanosheets and has a highly oriented microstructure (figure 2(d)). The high degree of overlap between graphene flakes enables efficient charge transport across the electrode and improved electrical performance, which are critical characteristics for electrochemical biosensors [57, 58, 73].

2.3. Spectral characterization

The chemical properties of the AJP graphene-based electrodes were characterized by Raman spectroscopy and x-ray photoelectron spectroscopy (XPS). Figure 2(e) presents the Raman spectrum of the AJP dipstick electrodes with the expected D, G, and 2D modes that are characteristic of graphene. The

IOP Publishing 2D Mater. **9** (2022) 035016 C C Pola et al

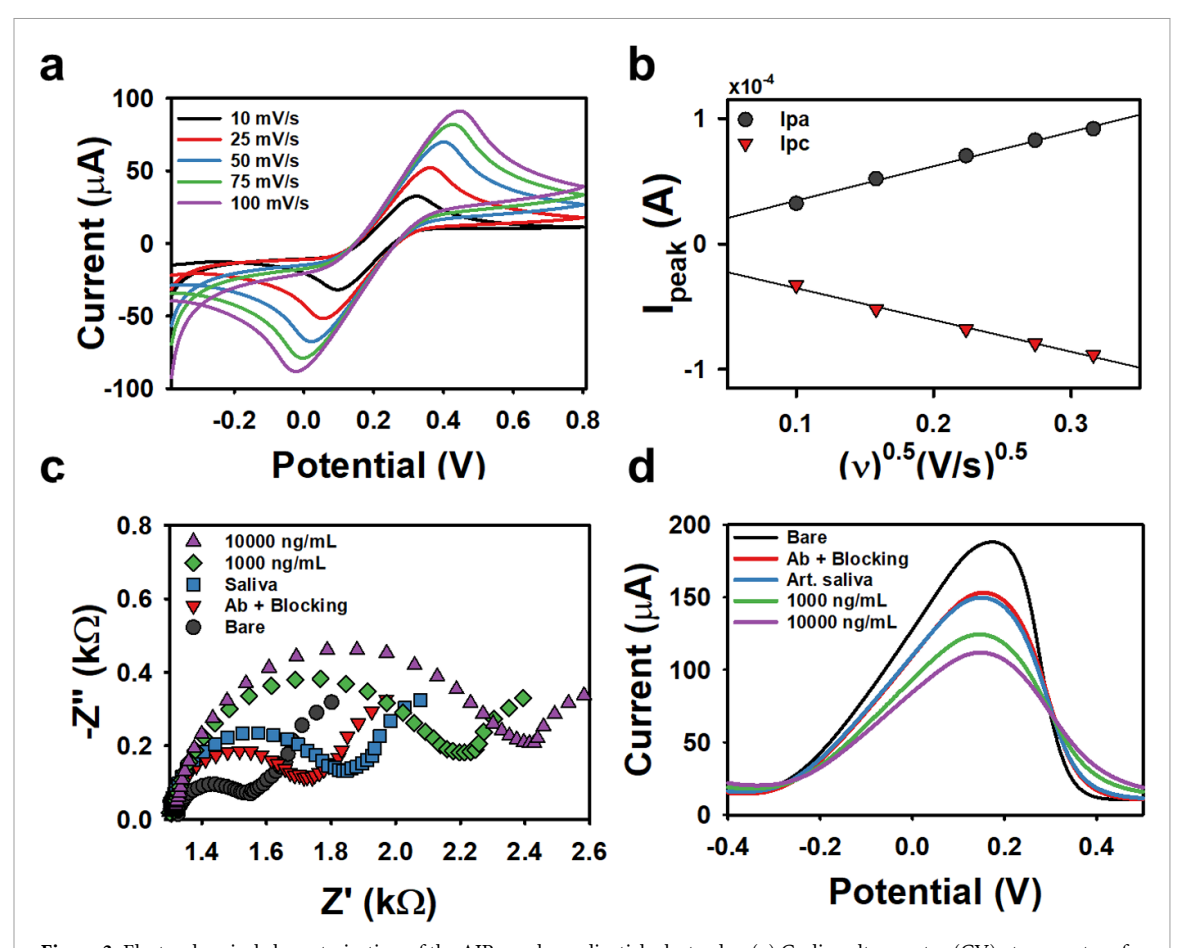


Figure 3. Electrochemical characterization of the AJP graphene dipstick electrodes. (a) Cyclic voltammetry (CV) at scan rates of 10, 25, 50, 75, 100 mV s⁻¹. (b) Randles–Sevcik plot showing a linear variation of the peak anodic (I_{pa}) and cathodic (I_{pc}) currents with square root of the scan rate with the resulting slope being used to calculate the ESA. (c), (d) Nyquist plot and DPV plot of the electrode after each biosensor experimental step: as-prepared AJP graphene electrode (bare), functionalization with SARS-CoV-2 spike rabbit polyclonal antibody (Ab) and surface blocking using Superblock[™], incubation with artificial saliva, and incubation with 1000 and 10 000 ng ml⁻¹ SARS-CoV-2 spike RBD, respectively.

first-order D peak, observed at 1341.14 cm⁻¹, is associated with the presence of lattice defects in the graphitic layers that results from breaks and bends in the sigma bonds [59, 75, 76]. The G peak, observed at 1576.47 cm^{−1}, occurs from in-plane vibrations of the sp²-bonded carbon atoms [57, 59, 73, 76]. Meanwhile, the second order 2D peak (2684.4 cm⁻¹) originates from the double resonance electron-phonon scattering characteristic of graphene [57, 58, 75]. The $I_{\rm 2D}/I_{\rm G}$ ratio was 0.36 \pm 0.03 and indicates the fewlayer nature of the graphene nanosheets [77, 78]. Additionally, the I_D/I_G peak intensity ratio, which is commonly used as a measure of disorder [75], was mapped across a 30 imes 30 μ m region of the electrode active area (figure 2(f)). The observed low I_D/I_G ratio (0.33 ± 0.025) indicates that the graphene nanosheets and EC carbonaceous residues are rich in sp² carbon and have a low defect density [73, 74]. Thus, the solution processing techniques of shear mixing, horn tip sonication, and AJP are capable of preserving the structural and chemical properties of graphene nanosheets.

The AJP graphene-based devices were further characterized using XPS to determine the functional

groups present on the surface of the electrode. XPS revealed a predominance (90.81%) of C–C sp² bonds, which are represented by the peak centered at a binding energy of 283.97 eV (figure 2(g)). Additionally, the presence of oxygen-containing moieties in the form of carbonyl groups (C=O) were observed at 290.57 eV (9.19%). The presence of oxygen functional groups on the surface of the graphene is beneficial for subsequent functionalization steps, since they are used as active sites to covalently link antibodies onto the electrode surface via the NHS-stabilized carbodimide EDC reaction as discussed below [79].

2.4. Electrochemical characterization

Next, the AJP graphene-based electrodes were electrochemically characterized to assess their suitability for biosensor applications. Cyclic voltammetry (CV) (figure 3(a)) was performed at different scan rates (10, 25, 50, 75, and 100 mV s⁻¹). The obtained curves presented well-defined anodic and cathodic peaks, which were observed between -0.05 and 0.47 V and increased linearly with the square root of the scan rate (figure 3(b)). The voltage peak separation also shifted with the scan rate, ranging from

223 to 533 mV, indicating limitations in the electron transfer. Such behavior is indicative of an irreversible system ($\Delta E_p > 200 \text{ mV}$) with slow electron transfer rate compared to mass transport [80-82]. Limitations in the electron transfer can be attributed to the low defect density and relatively planar surface [83], as corroborated by the Raman and SEM results, respectively (figures 2(d)–(f)). The electroactive surface area (ESA) was estimated using the Randles–Sevcik theorem as presented in equation S1 (see supplemental information (available online at stacks.iop.org/TDM/9/035016/mmedia)). The calculated ESA for the AJP electrodes was $9.27 \pm 0.64 \text{ mm}^2$ corresponding to an increase of 31% compared to the geometric area (7.07 mm²). The larger ESA may be explained by C=O defects on graphene nanosheets, the film roughness, and the high concentration of exposed graphene edge sites, all of which contribute to the surface area available for electrochemical reactions.

After confirming the electrochemical properties of the bare electrode, EIS (figure 3(c)) and DPV (figure 3(d)) techniques were employed to electrochemically characterize the stepwise process of functionalizing the graphene electrode surface with SARS-CoV-2 polyclonal antibodies (Ab) via carbodiimide cross-linking (Methods section) and incubating the resultant sensor with the analyte SARS-CoV-2 spike RBD, as illustrated in figure 1. As various functionalization and analyte components bind to the electrode surface, diffusion of the redox probe from the bulk electrolyte to the electrode surface is diminished. These changes to the electrode surface can be quantitatively tracked through EIS and DPV by monitoring the charge transfer resistance (R_{ct}) and peak current (I_{peak}) , respectively. In EIS, a frequency-dependent impedance response is obtained by applying a DC potential, relative to the reference electrode, with a fixed-amplitude AC component. By plotting the impedance data on a complex plane diagram, i.e. a Nyquist plot with axes of real vs imaginary impedance, a kinetically controlled semicircular region is visualized at high frequencies (low Z', low -Z'') [70, 84]. The diameter of this semicircle represents R_{ct} , and the diameter increases as the complexity of the electrode surface increases and diffusion rate to the surface decreases [84]. For DPV measurements, I_{peak} is obtained by applying a linear potential sweep superimposed with short pulses of small amplitude to the electrode and measuring the current immediately before and after each potential change [85, 86]. The peak current (I_{peak}) decreases as the diffusion rate of the redox probe to the electrode surface decreases due to bound species [40, 61, 86, 87].

While both EIS and DPV are informative electrochemical techniques and can be successfully applied to detect SARS-CoV-2 [61, 88–90], EIS presented a higher signal change compared to DPV for our

biosensors. This higher signal change is consistent with previous literature that has found EIS to be more sensitive to small changes in the surface composition compared to DPV [84, 91–93]. Hence, we focused on using EIS for electrochemical characterization during the subsequent biosensing experiments.

2.5. SARS-CoV-2 sensing

For sensing experiments, the AJP dipstick electrodes were first functionalized using EDC/NHS crosslinker to bind SARS-CoV-2 polyclonal antibody (see Methods section). SARS-CoV-2 spike RBD detection was then evaluated using EIS (figure 4). Sensor calibration was performed by serially incubating the dipstick electrodes in increasing concentrations of spike RBD in artificial saliva and performing EIS after each incubation (figure 4(a)). A normalized value of the change in charge transfer resistance (ΔR_{ct}) was obtained for each EIS measurement with respect to the baseline R_{ct} value for the same electrode before any incubation. Finally, a calibration curve was constructed by plotting $\Delta R_{\rm ct}$ against the incubation concentration (figure 4(c)). The AJP-based biosensor presented a linear sensing range from 1 to 1000 ng ml⁻¹ $(R^2 = 83.97\%, p_{\text{model}} = 0.000, p_{\text{lack-of-fit}} = 0.888), a$ sensitivity of 44.51 \pm 16.66 $\Omega/log(ng\,ml^{-1})$, and LOD of 22.91 \pm 4.72 pg ml⁻¹.

To evaluate the stability of the AJP biosensor in artificial saliva and assess the possibility of false positives or changes to the electrode surface that were not due to binding events of spike RBD, a baseline calibration study was performed. In particular, the AJP graphene biosensor was serially incubated in artificial saliva in 30 min increments, and an EIS measurement was performed after each period (figure 4(b)). After 150 min (five incubations) the biosensor presented a change in $R_{\rm ct}$ of approximately 15%. This change is considerably lower than the response to target analyte. Furthermore, since the electrode would only be incubated twice in actual tests (i.e. blank and sample), the baseline is only expected to change by \sim 5.4% in practice (figure 4(d)).

Next, the AJP graphene biosensor was also used to detect the entire SARS-CoV-2 spike S1 protein (figure 5(a)). The linear sensing range for SARS-CoV-2 spike S1 in artificial saliva was similar to that obtained for spike RBD—i.e. 1–1000 ng ml⁻¹ $(R^2 = 95.81\%, p_{\text{model}} = 0.000, p_{\text{lack-of-fit}} = 0.413),$ with a sensitivity of 36.92 \pm 9.31 $\Omega/\log(\text{ng ml}^{-1})$ and LOD of 110.38 \pm 9.00 pg ml⁻¹. Initially, SARS-CoV-2 spike S1 (molecular weight (MW) ~ 75 kDa) was expected to generate higher sensitivity than spike RBD (MW \sim 25 kDa), considering its higher molecular weight, which suggests that it would more efficiently block the electron transfer between the electrode surface and the electrolyte. However, the results indicated a higher sensitivity and lower LOD when only the SARS-CoV-2 spike RBD protein was used

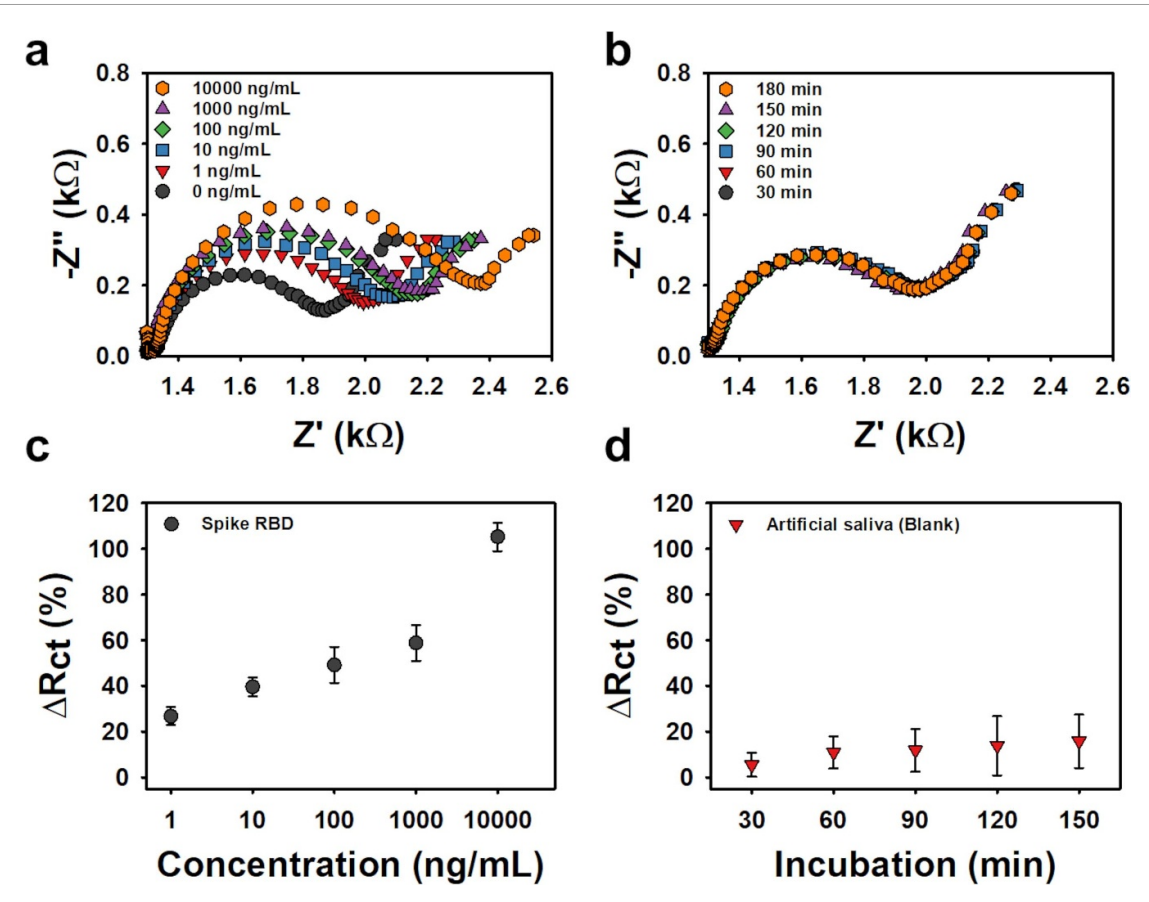


Figure 4. SARS-CoV-2 spike RBD detection in artificial saliva using AJP graphene sensors. (a) Representative Nyquist plots for each spike RBD concentration added to artificial saliva. (b) Representative Nyquist plot for the baseline over time—i.e. subsequent incubations of a functionalized electrode in artificial saliva without addition of spike RBD. (c) Calibration plot showing the percentage change of charge transfer resistance (ΔR_{ct}) with respect to spike RBD concentration ranging from 1 ng ml⁻¹ to 10 μ g ml⁻¹ in artificial saliva. (d) Calibration plot showing the percentage change of charge transfer resistance (ΔR_{ct}) for the subsequent incubations in artificial saliva. Error bars represent the standard deviation calculated from three independently biofunctionalized electrodes (n = 3).

as the antigen. Possibly, the efficacy of the antigenic interaction between the spike protein and the antibodies present on the surface of the AJP graphene biosensor depends on the conformation of the antigen protein [94, 95]. In addition, steric hindrance promoted by the neighboring high molecular weight spike S1 proteins could create a shielding effect on the antibody binding sites, compromising the strength of the antigenic interaction [23]. Therefore, the spike RBD is more accessible to interact with the recognition agent, effectively limiting the electron transfer and increasing the charge transfer resistance.

The selectivity and cross-reactivity of the AJP graphene biosensor was initially assessed by exposing it to Middle East respiratory syndrome (MERS)-CoV spike S1 protein. MERS-CoV is another type of coronavirus that also compromises the respiratory system. It was first reported in Saudi Arabia in 2012 and spread to 27 countries causing 888 deaths by July 2021 [96–98]. Unlike SARS-CoV-2, MERS-CoV presents a low human-to-human transmission rate, but its fatality rate is notably high (34.4%), especially when compared to the current rate reported for SARS-CoV-2 (1%–3%) [97, 98]. The AJP

graphene biosensor presented a considerable change in R_{ct} when incubated with MERS-CoV, reaching a maximum percentage change of 67.91 \pm 1.17%. In spite of the significant change in R_{ct} compared to the AJP graphene biosensor baseline (p = 0.001) at an antigen concentration of 10 000 ng ml⁻¹, the $\Delta R_{\rm ct}$ for MERS-CoV spike protein was still significantly lower than the ΔR_{ct} generated by both SARS-CoV-2 spike RBD (p = 0.001) and SARS-CoV-2 spike S1 (p = 0.007) at the same concentration. The moderate selectivity of the AJP graphene biosensor towards MERS-CoV is not highly concerning considering the limited number of cases outside of Saudi Arabia [99]. According to the CDC, MERS-CoV presents a negligibly low risk in the US, with only two positive cases since 2014 [100]. Moreover, according to Torrente-Rodríguez et al [61], the spike, envelope, and membrane proteins of SARS-CoV-2 share between 30% and 40% sequence identity with those of MERS-CoV, which implies that cross-reactivity should be expected. Another important factor is the use of polyclonal antibodies in functionalizing our AJP graphene electrodes. Polyclonal antibodies are produced by the natural immune response of multiple B-lymphocytes

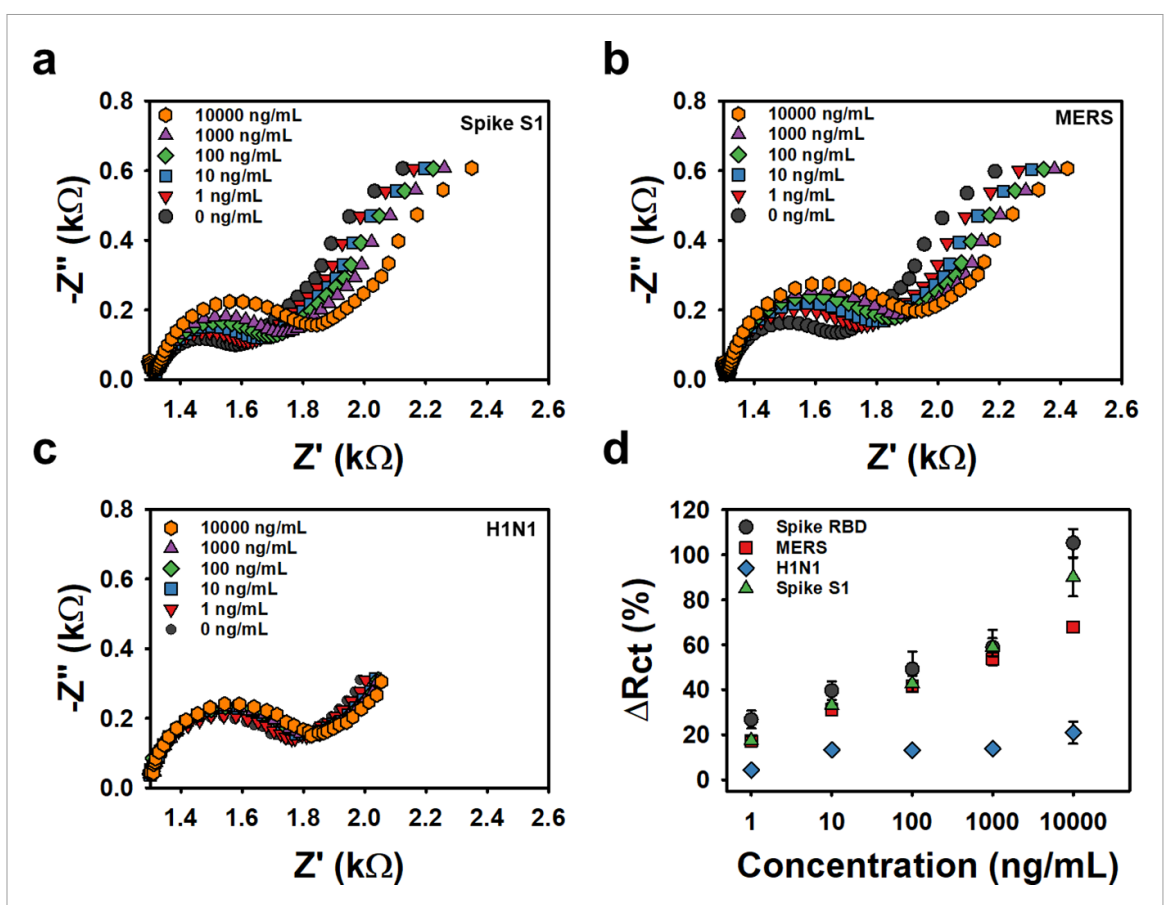


Figure 5. SARS-CoV-2 spike S1 and spike RBD detection in artificial saliva and against interferents using the AJP graphene sensor. (a) Representative Nyquist plots for each spike S1 concentration added to artificial saliva using the same concentration range tested previously for SARS-CoV-2 spike RBD. (b) Representative Nyquist plots for each concentration of Middle East respiratory syndrome (MERS) spike S1 added to artificial saliva. (c) Representative Nyquist plot for each concentration of influenza H1N1 hemagglutinin (HA) protein added to artificial saliva. (d) Calibration plot showing the percentage change of charge transfer resistance (ΔR_{ct}) observed at different concentrations of each protein tested, including spike RBD. Error bars represent the standard deviation calculated from three independently biofunctionalized electrodes (n = 3).

and target multiple epitopes of the same antigen. Hence, polyclonal antibodies are more prone to cross-react with antigens that present protein similarities [101–104]. From a different perspective, the moderate sensitivity of our AJP graphene SARS-CoV-2 biosensor to MERS-CoV indicates the multi-target capability of our sensor platform and offers an opportunity for application of these biosensors to detect MERS-CoV.

Next, the selectivity of the AJP graphene biosensor was further tested with Influenza H1N1 hemagglutinin (HA) protein. As some symptoms of COVID-19 and the common flu are the same, molecular testing is crucial to confirm a diagnosis [105]. Following the same sensing protocol as used for SARS-CoV-2 and MERS-CoV, negligible cross-reactivity was detected for H1N1 HA protein, presenting a maximum change in $R_{\rm ct}$ of 14.97 \pm 6.98% at 10 000 ng ml $^{-1}$. The change promoted by H1N1 was not significantly different (p=0.918) from the baseline drift presented by the AJP biosensor when tested with pristine artificial saliva (figure 4(d)).

Several COVID-19 sensing devices have been reported in the literature since the beginning of

the pandemic. A comparison of the AJP graphene immunosensor developed in this work with other SARS-CoV-2 electrochemical biosensors is summarized in table 1. The performance of the AJP graphene immunosensor is comparable to devices that presented a considerably more complex composition and additional fabrication steps. For example, Fabiani et al [38] reported an electrochemical immunosensor for detection of spike S1 and nucleocapsid protein in saliva samples using carbon black screen printed electrodes. Despite the use of MBs to pre-concentrate the sample before the DPV measurements, the device presented an LOD of 19 ng ml⁻¹ for spike S1. The label-free AJP graphene immunosensor developed here presented an LOD that is two orders of magnitude lower for spike S1 in artificial saliva for a similar incubation time (\sim 30 min). Other example include Yakoh et al [106], who developed an innovative paper-based graphene oxide sensor to detect spike RBD in saliva samples, and Vadlamani et al [40], who developed a rapid amperometric sensor functionalized with TiO2 nanotubes for the detection of spike RBD in saliva samples. Besides the extremely low response time and the need for decoration with

 Table 1. Comparison among different electrochemical biosensors for SARS-CoV-2 antigens detection.

Transducer	Technicus	Target	Media	$10D(m_{\rm s}{\rm m}^{1-1})$	Tinear concing range (ng ml-1)	Deeponee time	Doforoncos
Hallstucci	recumdae	ıaığıı	Mcdia	LOD (Pg mil.)	Luicai sciising range (ng m	mesponse unite	Weier critees
GO paper based	SWV—label free	RBD	Serum	110	$1-10^{3}$	NA	[106]
LSG	DPV	S	Blood serum	2.9×10^{3}	5-500	1 h	[63]
AuNP	Label-free SWV	Z	Nasopharyngeal	0.4	NA	NA	[107]
MNP/Carbon black SPE	DPV	S1	Buffer and Saliva	$1.4 \times 10^4 \text{ and } 1.9 \times 10^4$	$10-6.0 \times 10^2$	30 min	[38]
Co-TiO ₂ nanotube	Amperometry	RBD	Saliva	1.75×10^{4} a	$3.5 \times 10^2 - 3.5 \times 10^4$	30 s	[40]
RAPID1.0	EIS	Spike	Saliva	2.8×10^{-3}	$1-10^{6}$	1 min	[88]
Cu_2O NC SPE	EIS	S	Saliva, nasal and UTM	4.0×10^{-5}	$2.5 \times 10^{-7} - 1.0 \times 10^3$	20 min	[41]
AJP-graphene	EIS	RBD	Artificial saliva	22.91	$1-10^{3}$	33 min	This work
AJP-graphene	EIS	S1	Artificial saliva	110.38	$1-10^{3}$	33 min	This work

Techniques: graphene oxide (GO); square wave voltammetry (SWV); laser-Scribed Graphene (LSG); differential pulse voltammetry (DPV); magnetic nanoparticles (MNP); electrochemical impedance spectroscopy (ElS); Carbon electrode (CE), aerosol jet printed (AJP). Transducers: reduced graphene oxide (rGO); gold nanoparticles (AuNPs); carbon nanotubes (CNTs). Media: phosphate buffered saline (PBS); universal transport medium (UTM). ^a Considering the molecular weight of spike RBD as 25 kDa. TiO_2 nanotubes, their device only presented an LOD of 17.5 ng ml⁻¹ for spike RBD.

Despite the fast response time, high sensitivity, and user-friendly characteristics of some of the electrochemical sensors for SARS-CoV-2, their high cost and upscaling limitations have prevented their widespread use in the COVID-19 pandemic [108]. In contrast, the AJP graphene immunosensors developed in this work are economical, with an estimated cost of \$3.39 per unit (approximate cost breakdown: polyimide = 0.44; EDC:NHS = 0.03; Superblock = \$0.01; SARS-CoV-2 polyclonal antibody = \$2.90; AJP graphene-based ink = \$0.01). Limitations associated to the cross-reaction with MERS-CoV can be overcome by using monoclonal antibodies, which are specific to a single target analyte, during the functionalization step. Based on the overall performance of the AJP graphene immunosensor, this platform represents a cost-effective, sensitive, easy-to-use, and high-throughput approach that can be massively deployed for COVID-19 testing.

3. Conclusions

This work reports the successful development of an AJP graphene-based SARS-CoV-2 electrochemical immunosensor. The printed dipstick electrodes were highly conductive with a printed film thickness of 225 nm and an ESA that is 31% higher than the geometric area. The graphene electrodes were functionalized with SARS-CoV-2 Rabbit polyclonal antibody via EDC:NHS carbodiimide reaction, and detection of SARS-CoV-2 spike RBD was validated in artificial saliva without any labeling or pretreatment to resemble a real-life application of rapidly acquiring and testing a saliva sample from a patient. In just 33 min, the AJP graphene immunosensor could quantitatively detect SARS-CoV-2 spike proteins in artificial saliva within a wide linear sensing range spanning four orders of magnitude of the antigen concentration (1-1000 ng ml⁻¹) and an LOD of 22.91 \pm 4.72 pg ml $^{-1}$ for spike RBD and $110.38 \pm 9.00 \text{ pg ml}^{-1}$ for spike S1. Importantly, the AJP graphene immunosensor did not show crossreactivity to H1N1 HA protein while presenting a potential application as a multi-target device when MERS-CoV spike sensing is needed. Thus, the printed AJP graphene immunosensor not only provides a sensitive and rapid solution for COVID-19 testing, but also has the potential for widespread accessibility due to its fabrication using inexpensive, high-yield graphene production and high-throughput printing techniques. Since a test-and-trace strategy has been widely applied to fight the pandemic, this device can be used for on-site screening of potential COVID-19 patients, considerably increasing the number of tested cases, which is essential for the control of COVID-19 spread, especially in underdeveloped and developing countries. Ultimately, this device platform can

be broadly tuned for a multitude of targets such as COVID-19 variants, foodborne pathogens, biomarkers, and allergens, suggesting its widespread use in future electrochemical sensing applications.

4. Methods

4.1. Materials

Graphite flakes, EC (4 \times 10⁻³ Pa s⁻¹), terpineol, EDC, NHS, ethanolamine, 2-(N-morpholino) ethanesulfonic acid (MES) buffer, potassium hexacyanoferrate (II) trihydrate, and potassium ferricyanide, were purchased from MilliporeSigma (Saint Louis, MO, USA). Potassium chloride was purchased from Fisher Scientific (Hampton, NH, USA). Superblock™ buffer and 200-proof ethanol were purchased from Thermo Fisher (Waltham, MA, USA). Artificial saliva was purchased from Pickering Laboratories (Mountain View, CA, USA). Phosphate buffer saline was purchased from Alfa Aesar (Tewksbury, MA, USA). SARS-CoV-2 spike rabbit polyclonal antibody (Cat. #40591-T62), SARS-CoV-2 spike RBD protein (Cat. #40592-V08H), SARS-CoV-2 spike S1 protein (Cat. #40591-V08H), MERS spike S1 protein (Cat. #40069-V08H), and influenza H1N1 HA protein (Cat. #40006-V08H) were purchased from Sino Biological (Sino Biological US Inc., Wayne, PA, USA).

4.2. Graphene synthesis

First, a graphene powder was prepared according to a previously reported procedure [74]. Briefly, graphite flakes, EC, and ~20 l of ethanol were mixed in a weight ratio of 30:1:20 and processed for 24 h in a Silverson 200L high-shear in-line mixer at maximum power. The produced slurry was centrifuged, flocculated, washed, and dried to obtain a powder of exfoliated graphene nanosheets stabilized with EC. This procedure yields a standard batch of 40–50 g of graphene/EC powder containing ~40 wt% graphene for redispersion in organic solvents.

4.3. Graphene ink formulation

The graphene powder was redispersed in ethanol (10 mg ml⁻¹) by horn tip sonication at an amplitude of 10% for 1 h. The dispersion was filtered through a 3.1 μ m syringe filter to remove large aggregates. Finally, to formulate an aerosol-jet-printable ink, the graphene dispersion was mixed with terpineol at 9:1 (v/v) ratio and then again bath sonicated for 10 min prior to printing.

4.4. AJP

The graphene ink was aerosol jet printed using an Optomec AJ200 printer (Albuquerque, NM, USA). During printing, the ultrasonication bath was held at 30 °C and the printing bed was held at 60 °C. The ink was atomized by applying current between 0.3 and 0.35 mA onto the atomizer and was deposited with aid of nitrogen sheath flow and a nitrogen carrier flow

C C Pola et al

at rate between 40–60 sccm and 10–30 sccm, respectively. The printing speed was fixed at 5 mm s⁻¹, and the flow rates were tuned throughout each printing session to facilitate continuous deposition of graphene lines with widths of 40 μ m. To fabricate dipstick electrodes, the respective dipstick pattern was designed in AutoCAD and then printed in a single pass with a serpentine fill that had 30 μ m spacing between adjacent lines. After printing, the devices were heated at 350 °C for 30 min in air in a box furnace to evaporate residual solvent. Simultaneously, the heat treatment promoted the decomposition of EC to form a sp²-rich carbonaceous residue that increases the conductivity of the graphene film [44].

4.5. AFM

To obtain topographic characterization of the printed graphene films, AFM was performed using two systems: Asylum Cypher AFM (Oxford Instruments, Abingdon, UK) and Bruker Dimension Icon AFM (Bruker, Billerica, MA). Individual graphene nanosheets were characterized with the Cypher AFM in tapping mode using Si cantilevers with a resonance frequency of ∼320 kHz. AJP graphene films were characterized with the Bruker Dimension Icon AFM equipped with an OLTESPA-R3 cantilever and resonance frequency of 70 kHz in ScanAssyst tapping mode. Wide window scans (90 μ m) were acquired to characterize film thickness across a scratch imposed in the film. Scanning parameters were fixed at 1024 pixels/line and a 0.8 Hz scan rate. AFM scans were graphically processed with the use of Gwyddion software equipped with tools like scars removal, denoising, and background flattening. The height profile and surface statistical analysis tools in Gwyddion were also used to evaluate the roughness and thickness of the printed graphene films. To obtain statistical information for the graphene size distribution, an in-house MATLAB (MathWorks, Natick, MA, USA) image processing algorithm was used. This algorithm identifies the edges of nanosheets and creates a mask that individually labels each nanosheet. The mask can be adjusted by the user. Then the algorithm calculates the mean thickness, maximum length, area, and volume of each nanosheet. These data were used to create the histograms shown in figures S1(c) and (d).

4.6. Functionalization

The working area of the AJP graphene-based dipstick electrodes was functionalized using 0.4 M EDC and 0.1 M NHS prepared in 0.1 M MES buffer (pH 6.0) for 1 h at room temperature, as previously described by [57]. Then, the AJP electrodes were incubated overnight with SARS-CoV-2 spike rabbit polyclonal antibody solution (100 μ g ml⁻¹) in sterile 1× phosphate buffered saline (PBS). After the incubation, the surface of the electrode was blocked with SuperblockTM buffer for 1 h at room temperature to

eliminate any non-specific binding of SARS-CoV-2 protein. The functionalized dipstick electrodes were stored in $1 \times$ PBS at 4 °C until further testing.

4.7. SEM

The morphology of the AJP graphene-based electrodes was evaluated using SEM. SEM images of the electrodes were acquired using a FEI Quanta 250 FE-SEM (Thermo Fisher Scientific, OR, USA) at an accelerating potential of 10 kV, \sim 10 mm of working distance, and spot size of 3.0. Prior to imaging, the samples were coated with a 2 nm layer of Iridium using a turbo pump sputter coater. Optical images were obtained using a Zeiss Axio Zoom v16 (Carl Zeiss, Oberkochen, Germany) at magnifications of $6.5 \times$ and $25 \times$.

4.8. Raman spectroscopy

Raman spectra were obtained using a Horiba XploRa PLUS microscope (Horiba, Kyoto, Japan) with a 532 nm laser and 1800 mm $^{-1}$ grating. When measuring graphene samples deposited on polyimide, the FLAT correction was applied to remove the substrate background signal. Each spectrum was obtained with 10% laser power and averaged over 60 accumulations, each with an acquisition time of 1 s. To create a Raman map, spectra were acquired from a 30 $\mu m \times 30~\mu m$ region with 25 steps in each direction (1.25 μm between each point). To extract an accurate D/G peak intensity ratio, the D and G peaks were fit to Lorentzian curves.

4.9. XPS

Graphene films were characterized after thermal curing using XPS performed on a Thermo Scientific ESCALAB 250Xi (Thermo Fisher Scientific, Waltham, MA) that has an Al K α radiation source. Spectra for the C1s peak (279.2–298.2 eV with step size of 0.1 eV) was obtained in at least three spots per sample with a spot size of 500 μ m. Each XPS spectrum was fit in the Thermo Avantage software using the Knowledge Base graphene data as a guiding reference. Several fit variations were tested before concluding that the C1s spectrum was best fit with only two peaks representing the asymmetric C–C sp² signal and the C=O signal.

4.10. Electrochemical measurement

To verify the suitability of the AJP graphene electrode as a platform for electrochemical measurements, CV, DPV, and EIS were performed. The electrochemical measurements were carried out using a three-electrode set up with an Ag/AgCl reference electrode and a counter Pt wire on a PalmSens4 potentiostat (PalmSens, Utrecht, Netherlands). All measurements were carried out in 5 mM Fe(CN) $_6$ ³⁻/Fe(CN) $_6$ ⁴⁻ ferri/ferrocyanide (1:1) redox probe with 0.1 M KCl in 1× PBS. CV measurements were performed in a sweep range from -0.4 to 0.6 V with scan rates of

10, 25, 50, 75, and 100 mV. DPV measurements were performed in a potential range from -0.4 to 0.6 V, with 0.2 s of pulse width, 100 mV of pulse amplitude, and 4 mV incremental potential at a scan rate of 10 mV s⁻¹.

EIS measurements were carried out using a frequency range from 0.1 Hz to 10 kHz with an AC voltage amplitude of 5 mV and 0.2 V DC offset. The Nyquist plots were used to determine the charge transfer resistance ($R_{\rm ct}$), series resistance ($R_{\rm s}$), double-layer capacitance ($C_{\rm dl}$), and Warburg impedance ($Z_{\rm w}$) by fitting the data sets to the Randles-Ershler circuit model using the PSTrace 5.8 software.

4.11. SARS-CoV-2 sensing in artificial saliva

Sensing experiments were carried out to demonstrate the efficiency of the AJP graphene-based biosensor for the detection of SARS-CoV-2 spike protein. Standard solutions containing SARS-CoV-2 spike S1 RBD and spike S1 were prepared in artificial saliva in concentrations ranging from 1 ng ml⁻¹ to 10 μ g ml⁻¹ (40 pM-400 nM). AJP graphene-based electrodes were incubated with 15 μ l of each standard solution for 30 min to allow the interaction between the SARS-CoV-2 spike S1 RBD protein and the antibody immobilized on the surface of the electrode. Between each measurement, the electrodes were thrice washed with 100 μ l of 1× PBS to remove the residual ferro/ferricyanide. SARS-CoV-2 spike S1 RBD calibration plots were obtained by measuring the diameter of the semicircle obtained in the Nyquist plot, which corresponds to R_{ct} for each successive concentration using the same EIS parameters as described in section 4.10. To demonstrate the stability of the AJP graphene-based biosensor under successive incubations with artificial saliva over time, EIS measurements were performed under the same conditions described above without the presence of SARS-CoV-2 spike RBD protein.

4.12. Selectivity test

Considering the possible presence of interferent molecules in a saliva sample, the selectivity of this biosensor towards SARS-CoV-2 spike RBD and spike S1 was evaluated. MERS-CoV (spike S1) and influenza H1N1 (HA) proteins were selected as potential interferent molecules, considering similarities in protein structure and symptoms to SARS-CoV-2. The AJP graphene-based biosensors were incubated with different concentrations, ranging from 1 ng ml⁻¹ to 10 μ g ml⁻¹, of each protein in artificial saliva under the same conditions of the sensing experiments (section 4.5), and the change in $R_{\rm ct}$ generated by each protein during EIS measurements was evaluated.

4.13. Data analysis

A completely randomized design was used in this study with at least three replicates, and the results were reported as mean \pm standard deviation. Data

analysis was performed using JMP Pro statistical software (version 15, SAS, Cary, NC). Qualitative comparisons were carried out using one-way ANOVA and significantly different means (p < 0.05) were separated using Tukey's Honest Significant Differences test. Regression analysis with confidence level of 95% was performed to determine the linear sensing range and the functional correspondence among quantitative variables. Limits of detection for the biosensors were calculated using the 3σ method [109].

Data availability statement

All data that support the findings of this study are included within the article (and any supplementary files).

Acknowledgments

The authors thank Ana C M de Moraes for her assistance with ink rheology measurements. The authors gratefully acknowledge funding support for this work from the Centers for Disease Control and Prevention under Contract Number 75D30121C10238. Research reported in this publication was also supported by the National Institute on Alcohol Abuse and Alcoholism of the U S National Institutes of Health under Award Number U01AA029328. Graphene powder production was supported by the National Science Foundation Scalable Nanomanufacturing Program (NSF CMMI-1727846 and NSF CMMI-2039268) and the National Science Foundation Future Manufacturing Program (NSF CMMI-2037026). Aerosol jet printing was supported by the U S Department of Commerce, National Institute of Standards and Technology (Award 70NANB19H005) as part of the Center for Hierarchical Materials Design (CHiMaD). The content is solely the responsibility of the authors and does not necessarily represent the official views of the Centers for Disease Control and Prevention and National Institutes of Health. This work made use of the Keck-II facility of the Northwestern University NUANCE Center and the MatCI facility, which have received support from the SHyNE Resource (NSF ECCS-2025633), the IIN, and the Northwestern MRSEC program (NSF DMR-1720139). Figure 1 was created with BioRender.com.

Conflict of interest

The authors declare no competing financial interest.

ORCID iDs

Cícero C Pola https://orcid.org/0000-0001-6141-9698

Beata M Szydłowska https://orcid.org/0000-0003-1441-0919 Kshama W Parate https://orcid.org/0000-0002-0890-6689

Shay G Wallace https://orcid.org/0000-0002-7535-6138

Mark C Hersam https://orcid.org/0000-0003-4120-1426

Carmen L Gomes • https://orcid.org/0000-0003-0095-6478

Jonathan C Claussen https://orcid.org/0000-0001-7065-1077

References

- [1] WHO 2022 WHO Coronavirus (COVID-19) dashboard (available at: https://covid19.who.int/) (Accessed 30 March 2022)
- [2] Hristov D, Rijal H, Gomez-Marquez J and Hamad-Schifferli K 2021 Developing a paper-based antigen assay to differentiate between coronaviruses and SARS-CoV-2 spike variants *Anal. Chem.* 93 7825–32
- [3] Kaushik A K, Dhau J S, Gohel H, Mishra Y K, Kateb B, Kim N-Y and Goswami D Y 2020 Electrochemical SARS-CoV-2 sensing at point-of-care and artificial intelligence for intelligent COVID-19 management ACS Appl. Bio Mater. 3 7306–25
- [4] International Monetary Fund 2021 World Economic Outlook Update January 2021 (available at: www.imf.org/en/Publications/WEO/Issues/2021/01/26/2021-world-economic-outlook-update) (Accessed 10 January 2022)
- [5] UNESCO 2020 Adverse consequences of school closures vol 10 pp 1–2 (available at: https://en.unesco.org/covid19/ educationresponse/consequences) (Accessed 19 November 2021)
- [6] Fasano M V, Padula M, Má A, Avico A J, Sala M and Andreoli M F 2021 Consequences of lockdown during COVID-19 pandemic in lifestyle and emotional state of children in Argentina Front. Pediatr. 14 9
- [7] Van Dyke M E et al 2020 Morbility and Mortality Weekly Report Morbidity and mortality weekly report trends in county-level COVID-19 incidence in counties with and without a mask mandate-Kansas, June 1– August 23, 2020 (available at: www.cdc.gov/coronavirus/2019ncov/prevent-) (https://doi.org/ 10.15585/mmwr.mm6947e2) (Accessed 10 January 2022)
- [8] The New York Times 2022 The U.S. States that are ending mask mandates (available at: www.nytimes.com/explain/ 2022/03/01/us/mask-mandates-us) (Accessed 30 March 2022)
- [9] Congress 2021 (available at: www.congress.gov/bill/117thcongress/house-bill/375/text) (Accessed 30 March 2022)
- [10] New York State COVID-19 breakthrough data (available at: https://coronavirus.health.ny.gov/covid-19-breakthroughdata) (Accessed 30 March 2022)
- [11] The New York Times 2022 Tracking coronavirus vaccinations around the world (available at: www.nytimes. com/interactive/2021/world/covid-vaccinations-tracker. html) (Accessed 30 March 2022)
- [12] COVID.gov Get free at-home COVID-19 tests (available at: www.covid.gov/tests) (Accessed 30 March 2022)
- [13] AP News 2022 Shanghai starts China's biggest COVID-19 lockdown in 2 years (available at: https://apnews.com/ article/covid-china-locking-down-shanghai-b406df3a0 113b9be99273324fec2c12e) (Accessed 30 March 2022)
- [14] The New York Times 2022 I'm a U.S. citizen Where can I go? (available at: www.nytimes.com/article/coronavirus-travel-restrictions.html) (Accessed 30 March 2022)
- [15] Shlomowitz A and Feher M D 2014 Anxiety associated with self monitoring of capillary blood glucose Br. J. Diabetes 14 60–63

- [16] Regalado A 2021 We reviewed three at-home COVID tests The results were mixed (available at: www.technolog yreview.com/2021/05/04/1024450/at-home-covid-testreview-accuracy-binaxnow-lucira-ellume) (Accessed 23 November 2021)
- [17] Moisset X et al 2021 Nasopharyngeal swab-induced pain for SARS-CoV-2 screening: a randomised controlled trial of conventional and self-swabbing Eur. J. Pain 25 924–9
- [18] Diaz J and Simmons-Duffin S 2021 FDA authorizes 2 rapid, at-home coronavirus tests (available at: www.npr.org/sections/coronavirus-live-updates/2021/ 04/01/983318237/fda-approves-2-rapid-at-home-covidtests) (Accessed 23 November 2021)
- [19] FDA (Food and Drug Administration) 2020 Potential for false positive results with antigen tests for rapid detection of SARS-CoV-2—letter to clinical laboratory staff and health care providers (available at: www.fda.gov/medicaldevices/letters-health-care-providers/potential-falsepositive-results-antigen-tests-rapid-detection-sars-cov-2letter-clinical-laboratory) (Accessed 23 November 2021)
- [20] Kretschmer A, Kossow A, Grüne B, Schildgen O, Mathes T and Schildgen V 2021 False positive rapid antigen tests for SARS-CoV-2 in the real-world and their economic burden J. Infect. 84 248–288
- [21] Health L 2021 Lucira check it COVID-19 All-In-One test kit (Lucira) (available at: https://checkit.lucirahealth.com/) (Accessed 23 November 2021)
- [22] Inaba M, Higashimoto Y, Toyama Y, Horiguchi T, Hibino M, Iwata M, Imaizumi K and Doi Y 2021 Diagnostic accuracy of LAMP versus PCR over the course of SARS-CoV-2 infection *Int. J. Infect. Dis.* 107 195–200
- [23] Liu G and Rusling J F 2021 COVID-19 antibody tests and their limitations ACS Sens. 6 593–612
- [24] Vogels C B F et al 2021 SalivaDirect: a simplified and flexible platform to enhance SARS-CoV-2 testing capacity Med 2 263–80.e6
- [25] Iwasaki S $\it et\,al\,2020$ Comparison of SARS-CoV-2 detection in nasopharyngeal swab and saliva J. Infect. 81 e145–7
- [26] Matuck B F et al 2021 Salivary glands are a target for SARS-CoV-2: a source for saliva contamination J. Pathol. 254 239–43
- [27] Wyllie A L et al 2020 Saliva is more sensitive for SARS-CoV-2 detection in COVID-19 patients than nasopharyngeal swabs N Engl J Med 383 1283–6
- [28] Bastos M L, Perlman-Arrow S, Menzies D and Campbell J R 2021 The Sensitivity and costs of testing for SARS-CoV-2 infection with saliva versus nasopharyngeal swabs: a systematic review and meta-analysis *Ann. Intern. Med.* 174 501–10
- [29] Feng W et al 2020 Molecular diagnosis of COVID-19: challenges and research needs Anal. Chem. 92 10196–209
- [30] de Puig H, Bosch I, Gehrke L and Hamd-Schifferli K 2017 Challenges of the nano-bio interface in lateral flow and dipstick immunoassays *Trends Biotechnol*. 35 1169–80
- [31] Ainla A, Mousavi M P S, Tsaloglou M-N, Redston J, Bell J G, Fernández-Abedul M T and Whitesides G M 2018 Open-source potentiostat for wireless electrochemical detection with smartphones Anal. Chem. 90 6240–6
- [32] Jiang J, Wang X, Chao R, Ren Y, Hu C, Xu Z and Liu G L 2014 Smartphone based portable bacteria pre-concentrating microfluidic sensor and impedance sensing system Sens. Actuators B 193 653–9
- [33] Zhang D, Lu Y, Zhang Q, Liu L, Li S, Yao Y, Jiang J, Liu G L and Liu Q 2016 Protein detecting with smartphone-controlled electrochemical impedance spectroscopy for point-of-care applications Sens. Actuators B 222 994–1002
- [34] Sidhu R K, Cavallaro N D, Pola C C, Danyluk M D, McLamore E S and Gomes C L 2020 Planar interdigitated aptasensor for flow-through detection of listeria spp. in hydroponic lettuce growth media *Sensors* 20 1–21

- [35] Statista 2019 Sales of the leading blood-glucose meter brands in the United States in 2019 (in million U.S. dollars) (available at: www.statista.com/statistics/326855/bloodglucose-meter-brands-sales-in-the-us/#:~:text= Privatelabelblood-glucosemeters, million U.S. dollars is ales) (Accessed 23 November 2021)
- [36] Seo G et al 2020 Rapid detection of COVID-19 causative virus (SARS-CoV-2) in human nasopharyngeal swab specimens using field-effect transistor-based biosensor ACS Nano 14 5135-42
- [37] Ali M A et al 2021 Sensing of COVID-19 antibodies in seconds via aerosol jet nanoprinted reduced-grapheneoxide-coated 3D electrodes Adv. Mater. 33 1-15
- [38] Fabiani L et al 2021 Magnetic beads combined with carbon black-based screen-printed electrodes for COVID-19: a reliable and miniaturized electrochemical immunosensor for SARS-CoV-2 detection in saliva Biosens. Bioelectron. **171** 112686
- [39] Mahari S, Roberts A, Shahdeo D and Gandhi S 2020 eCovSens-ultrasensitive novel in-house built printed circuit board based electrochemical device for rapid detection of nCovid-19 antigen, a spike protein domain 1 of SARS-CoV-2 bioRxiv 10.1101/2020.04.24.059204 (Accessed 23 November 2021)
- [40] Vadlamani B S and Verma S C 2020 Functionalized TiO₂ nanotube-based electrochemical biosensor for rapid detection of SARS-CoV-2 Sensors 20 1-10
- Rahmati Z, Roushani M, Hosseini H and Choobin H 2021 Electrochemical immunosensor with Cu₂O nanocube coating for detection of SARS-CoV-2 spike protein Microchim. Acta 188 105
- [42] Idili A, Parolo C, Alvarez-Diduk R and Merkoçi A 2021 Rapid and efficient detection of the SARS-CoV-2 spike protein using an electrochemical aptamer-based sensor ACS Sens. 6 3093-101
- [43] Zhang Z et al 2021 High-affinity dimeric aptamers enable the rapid electrochemical detection of wild-type and B.1.1.7 SARS-CoV-2 in unprocessed Saliva Angew. Chem., Int. Ed. 60 24266-74
- [44] Secor E B, Prabhumirashi P L, Puntambekar K, Geier M L and Hersam M C 2013 Inkjet printing of high conductivity, flexible graphene patterns J. Phys. Chem. Lett. 4 1347-51
- [45] Song Y, Luo Y, Zhu C, Li H, Du D and Lin Y 2016 Recent advances in electrochemical biosensors based on graphene two-dimensional nanomaterials Biosens. Bioelectron. 76 195-212
- [46] Kuila T, Bose S, Mishra A K, Khanra P, Kim N H and Lee J H 2012 Chemical functionalization of graphene and its applications Prog. Mater. Sci. 57 1061-105
- [47] Yu H K, Balasubramanian K, Kim K, Lee J-L, Maiti M, Ropers C, Krieg J, Kern K and Wodtke A M 2014 Chemical vapor deposition of graphene on a "peeled-off" epitaxial Cu(111) foil: a simple approach to improved properties ACS Nano 8 8636-43
- [48] Russo P, Hu A, Compagnini G, Duley W W and Zhou N Y 2014 Femtosecond laser ablation of highly oriented pyrolytic graphite: a green route for large-scale production of porous graphene and graphene quantum dots Nanoscale 6 2381-9
- [49] Lin Y-M, Dimitrakopoulos C, Jenkins K A, Farmer D B, Chiu H-Y, Grill A and Avouris P 2010 100-GHz transistors from wafer-scale epitaxial graphene Science 327 662
- [50] Zaretski A V and Lipomi D J 2015 Processes for non-destructive transfer of graphene: widening the bottleneck for industrial scale production Nanoscale 7 9963-9
- [51] Shukla S, Kang S-Y and Saxena S 2019 Synthesis and patterning of graphene: strategies and prospects Appl. Phys. Rev. 6 021311
- [52] Hernandez Y et al 2008 High-yield production of graphene by liquid-phase exfoliation of graphite Nat. Nanotechnol. **3** 563–8

- [53] Ali M A, Hu C, Zhang F, Jahan S, Yuan B, Saleh M S, Gao S-J and Panat R 2022 N protein-based ultrasensitive SARS-CoV-2 antibody detection in seconds via 3D nanoprinted, microarchitected array electrodes J. Med. Virol. 94 2067-78
- [54] Li J, Wu D, Yu Y, Li T, Li K, Xiao -M-M, Li Y, Zhang Z-Y and Zhang G-J 2021 Rapid and unamplified identification of COVID-19 with morpholino-modified graphene field-effect transistor nanosensor Biosens. Bioelectron. 183 113206
- [55] El-Said W A, Al-Bogami A S and Alshitari W 2022 Synthesis of gold nanoparticles@reduced porous graphene-modified ITO electrode for spectroelectrochemical detection of SARS-CoV-2 spike protein Spectrochim. Acta A 264 120237
- [56] Zhang T, Sun L and Zhang Y 2021 Highly sensitive electrochemical determination of the SARS-COV-2 antigen based on a gold/graphene imprinted poly-arginine sensor Anal. Methods 13 5772-6
- [57] Parate K, Pola C C, Rangnekar S V, Mendivelso-Perez D L, Smith E A, Hersam M C, Gomes C L and Claussen J C 2020 Aerosol-jet-printed graphene electrochemical histamine sensors for food safety monitoring 2D Mater. 7 034002
- [58] Parate K, Rangnekar S V, Jing D, Mendivelso-Perez D L, Ding S, Secor E B, Smith E A, Hostetter J M, Hersam M C and Claussen J C 2020 Aerosol-jet-printed graphene immunosensor for label-free cytokine monitoring in serum ACS Appl. Mater. Interfaces 12 8592-603
- [59] Soares R R A et al 2020 Laser-induced graphene electrochemical immunosensors for rapid and label-free monitoring of Salmonella enterica in chicken broth ACS Sens. 5 1900-11
- [60] Cui T, Qiao Y, Gao J, Wang C, Zhang Y, Han L, Yang Y and Ren T-L 2021 Ultrasensitive detection of COVID-19 causative virus (SARS-CoV-2) spike protein using laser induced graphene field-effect transistor Molecules 26 6947
- [61] Torrente-Rodríguez R M, Lukas H, Tu J, Min J, Yang Y, Xu C, Rossiter H B and Gao W 2020 SARS-CoV-2 RapidPlex: a graphene-based multiplexed telemedicine platform for rapid and low-cost COVID-19 diagnosis and monitoring Matter 3 1981–98
- [62] Zhao H et al 2021 Ultrasensitive supersandwich-type electrochemical sensor for SARS-CoV-2 from the infected COVID-19 patients using a smartphone Sens. Actuators B 327 128899
- [63] Beduk T et al 2021 Rapid point-of-care COVID-19 diagnosis with a gold-nanoarchitecture-assisted laser-scribed graphene biosensor Anal. Chem. 93 8585-94
- [64] Muñoz J and Pumera M 2021 3D-printed COVID-19 immunosensors with electronic readout Chem. Eng. J. 425 131433
- [65] Grant B D, Anderson C E, Williford J R, Alonzo L F, Glukhova V A, Boyle D S, Weigl B H and Nichols K P 2020 SARS-CoV-2 coronavirus nucleocapsid antigen-detecting half-strip lateral flow assay toward the development of point of care tests using commercially available reagents Anal. Chem. 92 11305-9
- [66] He Q, Das S R, Garland N T, Jing D, Hondred J A, Cargill A A, Ding S, Karunakaran C and Claussen J C 2017 Enabling inkjet printed graphene for ion selective electrodes with postprint thermal annealing ACS Appl. Mater. Interfaces 9 12719-27
- [67] Das S R, Nian Q, Cargill A A, Hondred J A, Ding S, Saei M, Cheng G J and Claussen J C 2016 3D nanostructured inkjet printed graphene: via UV-pulsed laser irradiation enables paper-based electronics and electrochemical devices Nanoscale 8 15870-9
- [68] Hyun W J, Secor E B, Hersam M C, Frisbie C D and Francis L F 2015 High-resolution patterning of graphene by screen printing with a silicon stencil for highly flexible printed electronics Adv. Mater. 27 109-15

- [69] Secor E B, Lim S, Zhang H, Frisbie C D, Francis L F and Hersam M C 2014 Gravure printing of graphene for large-area flexible electronics Adv. Mater. 26 4533–8
- [70] Hondred J A, Stromberg L R, Mosher C L and Claussen J C 2017 High-resolution graphene films for electrochemical sensing via inkjet maskless lithography ACS Nano 11 9836–45
- [71] Hondred J A, Medintz I L and Claussen J C 2019 Enhanced electrochemical biosensor and supercapacitor with 3D porous architectured graphene via salt impregnated inkjet maskless lithography *Nanoscale Horiz.* 4 735–46
- [72] Secor E B 2018 Principles of aerosol jet printing Flex. Print. Electron. 3 035002
- [73] Secor E B, Gao T Z, Islam A E, Rao R, Wallace S G, Zhu J, Putz K W, Maruyama B and Hersam M C 2017 Enhanced conductivity, adhesion, and environmental stability of printed graphene inks with nitrocellulose *Chem. Mater.* 29 2332–40
- [74] De Moraes A C M, Obrzut J, Sangwan V K, Downing J R, Chaney L E, Patel D K, Elmquist R E and Hersam M C 2020 Elucidating charge transport mechanisms in cellulose-stabilized graphene inks J. Mater. Chem. C 8 15086–91
- [75] Childres I, Jauregui L A, Park W, Cao H and Chen Y P 2013 Raman spectroscopy of graphene and related materials New developments in photon and materials research Jang Joon Physics research technology (New York: Nova Science Publishers) 553–95
- [76] Pimenta M A, Dresselhaus G, Dresselhaus M S, Cançado L G, Jorio A and Saito R 2007 Studying disorder in graphite-based systems by Raman spectroscopy *Phys. Chem. Chem. Phys.* 9 1276–91
- [77] Wang Q H et al 2012 Understanding and controlling the substrate effect on graphene electron-transfer chemistry via reactivity imprint lithography Nat. Chem. 4 724–32
- [78] Nguyen V T, Le H D, Nguyen V C, Ngo T T T, Le D Q, Nguyen X N and Phan N M 2013 Synthesis of multi-layer graphene films on copper tape by atmospheric pressure chemical vapor deposition method Adv. Nat. Sci. Nanosci. Nanotechnol. 4 035012
- [79] Chiu N F, Fan S Y, Du Y C and Huang T Y 2017 Carboxyl-functionalized graphene oxide composites as SPR biosensors with enhanced sensitivity for immunoaffinity detection *Biosens*. *Bioelectron*. 89 370–6
- [80] Laviron E 1979 General expression of the linear potential sweep voltammogram in the case of diffusionless electrochemical systems *J. Electroanal. Chem.* 101 19–28
- [81] Lavagnini I, Antiochia R and Magno F 2004 An extended method for the practical evaluation of the standard rate constant from cyclic voltammetric data *Electroanalysis* 16 505–6
- [82] Vanegas D C, Patiño L, Mendez C, de Oliveira D A, Torres A M, Gomes C L and McLamore E 2018 Laser scribed graphene biosensor for detection of biogenic amines in food samples using locally sourced materials Biosensors 8 42
- [83] Zhang L, Liu H, Zhao Y, Sun X, Wen Y, Guo Y, Gao X, Di C-A, Yu G and Liu Y 2012 Inkjet printing high-resolution, large-area graphene patterns by coffee-ring lithography Adv. Mater. 24 436–40
- [84] Randviir E P and Banks C E 2013 Electrochemical impedance spectroscopy: an overview of bioanalytical applications Anal. Methods 5 1098–115
- [85] Cesewski E and Johnson B N 2020 Electrochemical biosensors for pathogen detection *Biosens. Bioelectron*. 159 112214
- [86] Molazemhosseini A, Magagnin L, Vena P and Liu C-C 2016 Single-use disposable electrochemical label-free immunosensor for detection of glycated hemoglobin (HbA1c) using differential pulse voltammetry (DPV) Sensors 16 1024

- [87] Su S, Cao W, Liu W, Lu Z, Zhu D, Chao J, Weng L, Wang L, Fan C and Wang L 2017 Dual-mode electrochemical analysis of microRNA-21 using gold nanoparticle-decorated MoS₂ nanosheet *Biosens*. *Bioelectron*. 94 552–9
- [88] Torres M D T, de Araujo W R, de Lima L F, Ferreira A L and de la Fuente-nunez C 2021 Low-cost biosensor for rapid detection of SARS-CoV-2 at the point of care *Matter* 4 2403–16
- [89] Ehsan M A, Khan S A and Rehman A 2021 Screen-printed graphene/carbon electrodes on paper substrates as impedance sensors for detection of coronavirus in nasopharyngeal fluid samples *Diagnostics* 11 1030
- [90] Mojsoska B, Larsen S, Olsen D A, Madsen J S, Brandslund I and Alatraktchi F A 2021 Rapid SARS-CoV-2 detection using electrochemical immunosensor Sensors 21 1–11
- [91] Garrote B L, Santos A and Bueno P R 2019 Perspectives on and precautions for the uses of electric spectroscopic methods in label-free biosensing applications ACS Sens. 4 2216–27
- [92] Bogomolova A, Komarova E, Reber K, Gerasimov T, Yavuz O, Bhatt S and Aldissi M 2009 Challenges of electrochemical impedance spectroscopy in protein biosensing Anal. Chem. 81 3944–9
- [93] Lisdat F and Schäfer D 2008 The use of electrochemical impedance spectroscopy for biosensing *Anal. Bioanal. Chem.* 391 1555–67
- [94] Janissen R et al 2017 InP nanowire biosensor with tailored biofunctionalization: ultrasensitive and highly selective disease biomarker detection Nano Lett. 17 5938–49
- [95] Kirchdoerfer R N et al 2018 Stabilized coronavirus spikes are resistant to conformational changes induced by receptor recognition or proteolysis Sci. Rep. 8 1–11
- [96] WHO 2021 Middle East respiratory syndrome coronavirus (MERS-CoV) (Saudi Arabia) (available at: www.who.int/ emergencies/disease-outbreak-news/item/2021-DON333)
- [97] Suarez D L, Pantin-jackwood M J, Swayne D E, Lee S A and Deblois S M 2020 Emerging Infect. Dis. 26 3074–6
- [98] Abdelrahman Z, Li M and Wang X 2020 Comparative review of SARS-CoV-2, SARS-CoV, MERS-CoV, and influenza a respiratory viruses Front. Immunol. 11 552909
- [99] Guo K et al 2021 Rapid single-molecule detection of COVID-19 and MERS antigens via nanobody-functionalized organic electrochemical transistors Nat. Biomed. Eng. 5 666–77
- [100] CDC 2019 MERS in the U.S. (available at: www.cdc.gov/ coronavirus/mers/us.html) (Accessed 12 November 2021)
- [101] Busby M et al 2016 Systematic comparison of monoclonal versus polyclonal antibodies for mapping histone modifications by ChIP-seq Epigenetics Chromatin 9 1–16
- [102] Wootla B, Denic A and Rodriguez M 2014 Polyclonal and monoclonal antibodies in clinic *Human Monoclonal Antibodies: Methods and Protocols* vol 1060 Steinitz Michael Methods Mol. Biol. (New Jersey: Humana Totowa) pp 79–110
- [103] Lipman N S, Jackson L R, Trudel L J and Weis-Garcia F 2005 Monoclonal versus polyclonal antibodies: distinguishing characteristics, applications, and information resources *ILAR J.* 46 258–67
- [104] Abcam 2021 (available at: www.abcam.com/protocols/acomparison-between-polyclonal-and-monoclonal) (Accessed 10 November 2021)
- [105] CDC 2021 Similarities and differences between flu and COVID-19 (available at: www.cdc.gov/flu/symptoms/fluvs-covid19.htm) (Accessed 10 November 2021)
- [106] Yakoh A, Pimpitak U, Rengpipat S, Hirankarn N, Chailapakul O and Chaiyo S 2021 Paper-based

2D Mater. **9** (2022) 035016 C C Pola et al

electrochemical biosensor for diagnosing COVID-19: detection of SARS-CoV-2 antibodies and antigen *Biosens*. *Bioelectron*. **176** 112912

- [107] Eissa S, Alhadrami H A, Al-Mozaini M, Hassan A M and Zourob M 2021 Voltammetric-based immunosensor for the detection of SARS-CoV-2 nucleocapsid antigen *Microchim. Acta* 188 199
- [108] Szunerits S et al 2021 The role of the surface ligand on the performance of electrochemical SARS-CoV-2 antigen biosensors Anal. Bioanal. Chem. 414 103–13
- [109] McNaught A D and Wilkinson A 1997 Compendium of Chemical Terminology—The Gold Book: IUPAC Recomendations 2nd edn (Oxford: Blackwell Scientific Publications) p 464